

Angle-resolved photoemission spectroscopy study of a system with a double charge density wave transition: ErTe₃

Seungho Seong¹, Heejung Kim,² Kyoo Kim,³ B. I. Min,² Y. S. Kwon,⁴ Sang Wook Han,⁵ Byeong-Gyu Park,⁶ R. Stania,^{6,7} Yeonji Seo,¹ and J.-S. Kang^{1,*}

¹Department of Physics, The Catholic University of Korea, Bucheon 14662, Korea

²Department of Physics, Pohang University of Science and Technology (POSTECH), Pohang 37673, Korea

³Korea Atomic Energy Research Institute (KAERI), Daejeon 34057, Republic of Korea

⁴Department of Emerging Materials Science, DGIST, Daegu 42988, Korea

⁵Basic Science Research Institute, University of Ulsan, Ulsan 44610, Korea

⁶Pohang Accelerator Laboratory (PAL), POSTECH, Pohang 37673, Korea

⁷Center for Artificial Low Dimensional Electronic Systems, Institute for Basic Science (IBS), Pohang 37673, Korea



(Received 16 September 2021; revised 17 November 2021; accepted 18 November 2021; published 29 November 2021)

The electronic structures of ErTe₃, having double charge density wave (CDW) transitions, have been investigated by performing polarization- and temperature (T)-dependent angle-resolved photoemission spectroscopy (ARPES) and Er $4d \rightarrow 4f$ resonant PES measurements for high-quality single crystals. It is found that Er $4f$ electrons do not contribute directly to CDW formation. The shadow Fermi surfaces (FSs) are clearly observed, arising from band folding due to the interlayer interaction. Twofold symmetric FS, but with weak FS reconstruction, is observed in the CDW phase of ErTe₃, which is similar to that of PrTe₃ having the CDW modulation vector $Q \approx 5/7 c^* \approx 5/7 a^*$. Very good agreement is found between the constant energy maps and ARPES measured in the CDW phase and the density functional theory band calculation for the non-CDW phase, implying very weak and only partial CDW-induced FS reconstruction in ErTe₃. Very weak and similar circular dichroism is observed along different symmetry lines in both FS and ARPES, suggesting weak chiral orbital and spin polarizations in the Te $5p$ orbitals. T -dependent FS and ARPES measurements reveal closing of the CDW gap on heating but no clear changes across T_{CDW2} and T_{CDW1} , supporting the very weak CDW distortion in ErTe₃. The origin of the very weak CDW reconstruction in ErTe₃ is likely to be the small ionic sizes of Er ions and the concomitant small volume that give rise to the imperfect FS nesting and the reduced density of states at the Fermi level. The very weak FS reconstruction at the first CDW transition along c^* is considered to be a reason why there exists a second CDW transition further along a^* , which elucidates the observed double CDW transitions in ErTe₃.

DOI: [10.1103/PhysRevB.104.195153](https://doi.org/10.1103/PhysRevB.104.195153)

I. INTRODUCTION

The charge-density wave (CDW) phase transition is one of the interesting phase transitions in nature [1–4]. The CDW transitions in the low-dimensional systems are considered to arise from Fermi surface (FS) instability, similar to the Peierls transition in one dimension (1D) [2] but also to involve more complicated physics. Quasi-2D transition-metal (M) chalcogenides, such as $1T$ - MX_2 or $2H$ - MX_2 ($X = S, Se, Te$) [5–7], are studied very extensively as CDW compounds where the electrons responsible for the CDW transition are M $3d$ electrons. Other interesting CDW compounds are layered rare-earth (R) tellurides of RTe_3 [8–12] in which the electrons responsible for the CDW transition are Te $5p$ electrons. Hence the electronic structures of RTe_3 seem to be simpler than those of MX_2 because the on-site Coulomb interaction (U) among Te $5p$ electrons is much weaker than that among M $3d$

electrons, which serves as an advantage of studying RTe_3 in the aspect of electronic structures.

An interesting feature in RTe_3 is that they exhibit two-step CDW transitions for heavy R elements, in contrast to the single-step CDW transition for light R elements [10,11,13–15]. To understand the origin of the CDW transitions in RTe_3 , extensive investigations have been reported for their electronic structures [13–20]. But the origin of different CDW transitions between light and heavy R elements in RTe_3 has not been clearly understood yet. Further, the systematic investigation of R $4f$ electrons in RTe_3 is lacking.

In this work we have investigated the electronic structure of ErTe₃ by employing angle-resolved photoemission spectroscopy (ARPES) and using high-quality stoichiometric single crystals. ARPES is a very powerful tool for studying the electronic structures of CDW compounds [5]. In particular, we have performed polarization- and temperature (T)-dependent ARPES as well as Er $4d \rightarrow 4f$ resonant PES (RPES) measurements. We have chosen ErTe₃ as a typical heavy RTe_3 system, which exhibits two CDW transitions

*kangjs@catholic.ac.kr

at well-separated temperatures, $T_{CDW1} = 265$ K and $T_{CDW2} = 155$ K [10,11,13–15].

II. EXPERIMENTAL DETAILS

ErTe_3 single crystals were grown by using a Te-flux, as described elsewhere for $R\text{Te}_3$ compounds [21]. From x-ray diffraction measurements, it was found that ErTe_3 crystallized in the C_{mcm} space group orthorhombic structure with lattice constants $a \approx c \approx 4.29$ Å and $b \approx 25.30$ Å at $T = 300$ K, which are similar to previously reported results [14,22].

ARPES measurements were carried out at 4A1 and 4A2 undulator beamlines of the Pohang Light Source by using Scienta R4000 and DA-30 electron energy analyzers, respectively. Single crystalline samples were cleaved *in situ* by using the top-post method at $T \approx 80$ K and measured under a pressure of better than 5×10^{-11} Torr at 4A1 and 2×10^{-10} Torr at 4A2. The cleaved surfaces were very shiny. Optical microscopy measurements, done after ARPES measurements, confirmed that the ARPES data presented in this work were obtained from flat regions. The Fermi level (E_F) and the instrumental resolution of the system were determined from the Fermi-edge spectrum of Au metal. The energy resolution (ΔE) and the momentum resolution (Δk) of the data presented in this work are better than $\Delta E < \sim 40$ meV and $\Delta k < 0.002$ Å⁻¹, respectively, at $h\nu \sim 70$ eV ($h\nu$: photon energy). All the spectra were normalized to the incident photon flux.

For density functional theory (DFT) band calculation, we employed the *ab-initio* full-potential linearized augmented band method implemented in Blaha *et al.* [23]. The generalized gradient approximation was utilized for the exchange-correlation interaction, and the spin-orbit interaction was taken into account in the second variation manner. For the DFT band structures below, Er 4*f* electrons were treated as core electrons by using the “4*f* open-core” method.

III. RESULTS AND DISCUSSION

Figure 1(a) shows the angle-integrated valence-band PES spectra of ErTe_3 employing Er 4*d* → 4*f* RPES [24]. Resonance enhancement due to the Er 4*d* → 4*f* absorption is observed around $h\nu \approx 174 - 176$ eV compared with those obtained well away from resonance (for example, see $h\nu = 127$ and 104 eV). The peaks in -12 eV $\lesssim E_i \lesssim -6$ eV (E_i : the initial-state energy), which exhibit strong resonance enhancement in the Er 4*f* on-resonance spectra, represent Er 4*f* states while those in -5 eV $\lesssim E_i \lesssim E_F$ represent Te 5*p* states, which become stronger well away from the Er 4*f* resonance [see $h\nu = 104$ eV in Fig. 1(a)].

As shown in Fig. 1(b), the Er 4*f* multiplet peaks between -5 and -12 eV represent the trivalent Er 4*f*¹¹ → 4*f*¹⁰ transition. This argument is supported by the similarity between the 4*f*¹⁰ final-state multiplets in ErTe_3 and those in other trivalent Er materials [25,26]. The peak positions of the Er 4*f* states are located well below E_F , indicating that Er 4*f* electrons are very localized. Further, the Er 4*f* spectral intensity at E_F is very weak in ErTe_3 . This finding suggests that the effect of Er 4*f* electrons on the CDW distortion in ErTe_3 would be negligible because the metallic electronic states near E_F

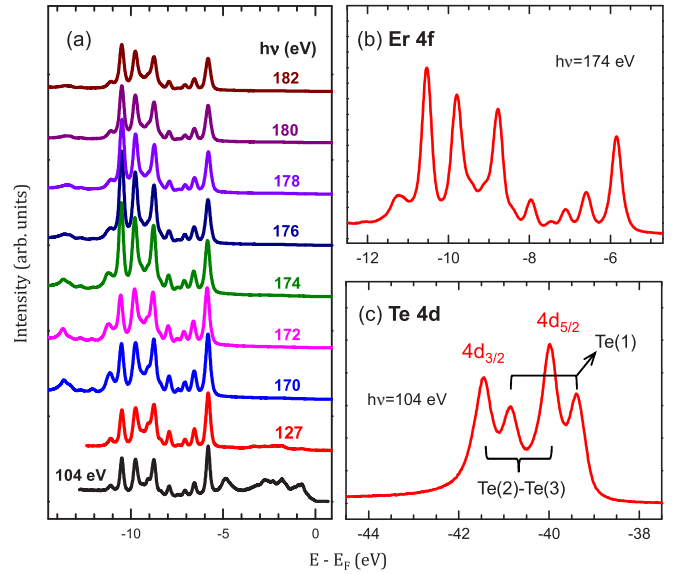


FIG. 1. Er 4*f* and Te 4*d* core-level PES spectra of ErTe_3 . (a) Er 4*f* PES spectra, including Er 4*d* → 4*f* RPES. (b) Er 4*f* PES spectrum obtained at $h\nu = 174$ eV. (c) Te 4*d* PES spectrum, obtained at $h\nu = 104$ eV. All data were obtained at $T \approx 80$ K.

in the non-CDW (normal) metallic phase are important in determining the CDW distortion, probably via FS nesting.

Figure 1(c) shows the Te 4*d* core-level PES spectrum of ErTe_3 , which exhibit two pairs of the spin-orbit (SO) split 4*d*_{5/2} and 4*d*_{3/2} components. We interpret these double peaks due to two different Te sites [see Fig. 2(a)], i.e., those at Er-Te(1) layers (low-BE peaks) and those at Te(2)-Te(3) sheets (high-BE peaks), respectively (BE: the binding energy, $BE = |E_i|$). Considering that there are two Te atoms in the Te(2)-Te(3) planar sheets and there is one Te atom in the Er-Te(1) layer per formula unit (f.u.), the weaker intensity of the low-BE peaks supports this assignment. This assignment is also confirmed by the DFT calculation [27]. The *bulk* and *surface* components may also contribute to the double-peak structures [28], but this contribution seems to be small in ErTe_3 because the measured Te 4*d* spectra were found to be rather similar for different cleaves [29].

Since Er ions are trivalent in ErTe_3 , an Er^{3+} ion donates three valence electrons per f.u.. Then it is expected that two electrons go to the Te ions in the Er-Te(1) double layer and 0.5 electron goes to each Te ion in the Te(2)-Te(3) layer [see Fig. 2(a)]. This will produce hole carriers in the Te(2)-Te(3) sheets [30], resulting in the ionic configuration of $\text{Er}^{3+}\text{Te}(1)^{2-}\text{Te}(2)^{0.5-}\text{Te}(3)^{0.5-}$. Due to the partial filling in Te(2)-Te(3) planes, the square nets of the Te(2)-Te(3) sheets are likely to be distorted by the Peierls-like mechanism [31]. This view is accepted theoretically [32–34] and experimentally [35,36].

Figure 2 shows the FS and constant energy (CE) slices of the angle maps of ErTe_3 for the *ac* plane obtained at $T \approx 80$ K and at $h\nu = 76$ eV by using the linear horizontal (LH) polarization. The measurement geometry for the LH polarization is shown in Fig. 3(a). Figures 2(a) and 2(b) show the orthorhombic structure of ErTe_3 and the schematic FS for the non-CDW phase (denoted in blue solid lines) on the 2*D* BZ

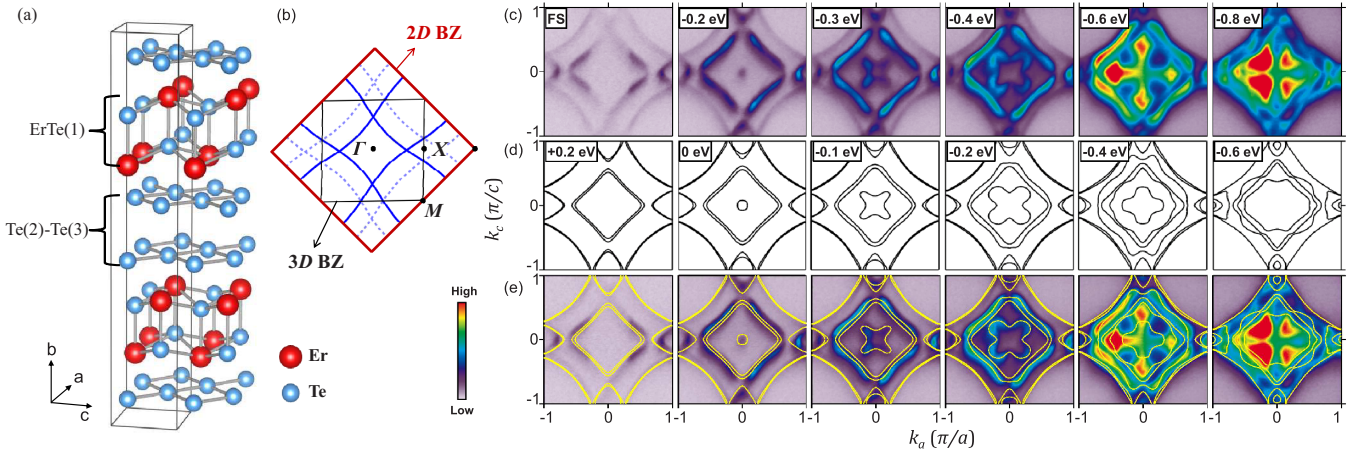


FIG. 2. Crystal structure, schematic FS, and CE maps for ErTe_3 . (a) Orthorhombic structure of ErTe_3 . (b) The schematic FS for the undistorted (non-CDW) phase of ErTe_3 (plotted in blue solid lines on the 2D BZ) and the folded-shadow FS (plotted in blue dotted lines on the 3D BZ). See the main text for the details. (c) The measured FS/CE maps of ErTe_3 for the k_a - k_c plane in the momentum space for the 3D BZ [denoted as black lines in (b)]. The labels denote the initial-state energies (E_i 's), which vary from $E_i = 0 \text{ eV}$ ($=E_F$) to $E_i = -0.8 \text{ eV}$. These were obtained at $h\nu = 76 \text{ eV}$ by using the LH polarization. (d) The calculated FS/CE maps obtained from the DFT calculation for the non-CDW phase of ErTe_3 . (e) Comparison of the measured and calculated FS/CE maps superposed onto each other. In this comparison, the calculated maps are cut at higher E_i 's by $+0.2 \text{ eV}$ compared with the measured maps.

and the shadow FS (denoted in blue dotted lines) folded into the 3D BZ, respectively. In orthorhombic ErTe_3 , the ac unit cell includes the doubled $\text{Te}(2)\text{-Te}(3)$ square net ($\sqrt{2} \times \sqrt{2}$) with respect to the original $\text{Te}(2)\text{-Te}(3)$ square lattice (1×1) due to the interlayer interaction between the $\text{Er}\text{-Te}(1)$ and the $\text{Te}(2)\text{-Te}(3)$ layers. Consequently, the shadow bands appear due to the folding of the bands of the original 2D BZ into the reduced 3D BZ, causing two diamond-shaped FSs in the 3D BZ. The larger outer-diamond FS represents the shadow

FS folded into the reduced 3D BZ, which arises from the folding of the bands in the outer 2D BZ into the inner-3D BZ [20]. Hence the outer-diamond FS is weaker than the inner-diamond FS in the first 3D BZ (centered at Γ) and vice versa in the second 3D BZ.

In Figs. 2(c)–2(e), the horizontal and vertical directions are along k_a (100) and k_c (001), respectively. Here the initial-state energy (E_i) varies from $E_i = 0 \text{ eV}$ (corresponding to E_F) to $E_i = -0.8 \text{ eV}$. The FS/CE maps in this figure were made

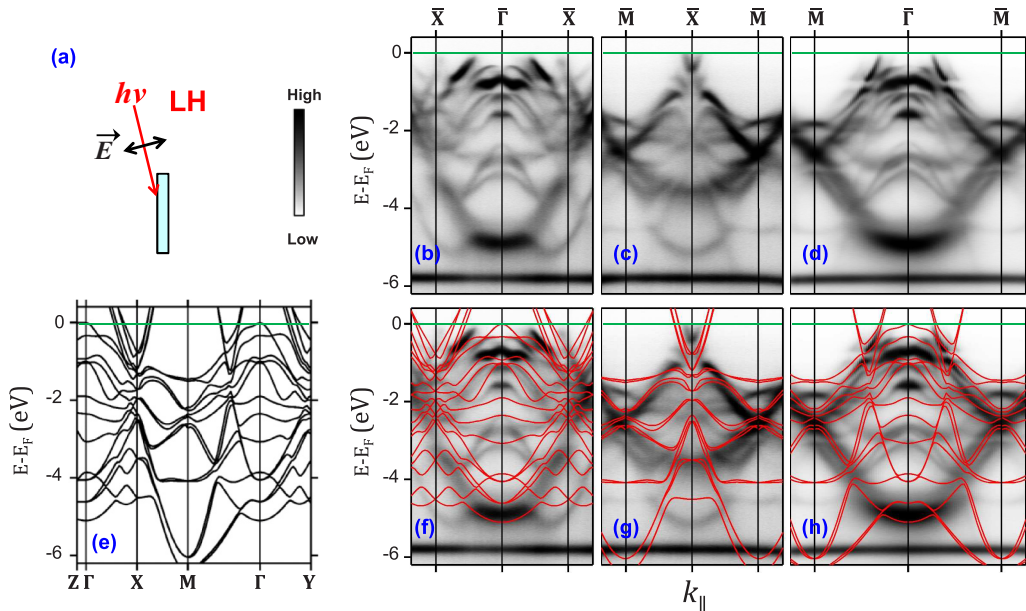


FIG. 3. Comparison between ARPES and the calculated band structures. (a) Schematic drawing for the LH polarization geometry. (b)–(d) ARPES image plots of ErTe_3 along $\bar{X}\bar{\Gamma}\bar{X}$, $\bar{M}\bar{X}\bar{M}$, and $\bar{M}\bar{\Gamma}\bar{M}$, respectively, obtained at $h\nu = 104 \text{ eV}$ by using the LH polarization and at $T \approx 80 \text{ K}$. (e) Calculated band structures along several high-symmetry lines obtained from the DFT calculation. (f)–(h) Comparison between ARPES and calculated band structures along $\bar{X}\bar{\Gamma}\bar{X}$, $\bar{M}\bar{X}\bar{M}$, and $\bar{X}\bar{M}\bar{X}$, respectively.

by integrating the spectral intensity of $E_i \pm 10$ meV for each E_i . The measured FS reveals two diamond-shaped FSs of a smaller (inner) FS and a larger (outer) FS. As explained in Fig. 2(b), these two FSs, exhibiting different intensities, do not represent the CDW distortion but they arise from the folding of the 2D BZ into the 3D BZ. Almost fourfold rotational symmetry is seen in the CE maps for $E_i \lesssim -0.2$ eV, indicating that the measured CE maps represent those by the Te square nets in the Te(2)-Te(3) sheets. In contrast, nearly twofold symmetric FS is observed, which is similar to but weaker than that of PrTe₃ [20]. This suggests that the local CDW modulation in ErTe₃ is similar to that in PrTe₃, even though the CDW distortion is weaker in ErTe₃.

Figure 2(d) shows the calculated FS/CE maps of ErTe₃ obtained from the DFT calculation for the non-CDW phase (i.e., normal metallic phase of ErTe₃). The observed splitting in the calculated FS/CE maps arises from both the mutual interaction of Te bilayers and the SO coupling of Te 5*p* electrons, but the former effect is dominating for the FS splitting. The trend in the measured CE slices with increasing $|E_i|$ agrees very well with that in the calculated CE maps. In particular, if one uses the calculated CE maps that are sliced at higher E_i 's by $\sim +0.2$ eV, they reveal very good agreement with the measured CE maps, which is shown more clearly in Fig. 2(e) where the measured and calculated FS/CE maps are superposed onto each other. The calculated FS/CE maps agree very well with the measured FS/CE, even though the splitting of Te bilayers is not resolved in the measured FS/CE data. But the predicted small bilayer splitting is within the width of the measured FS/CE data, and so this discrepancy does not conflict with the good agreement between calculations and experiment. The good agreement in the shape of CE maps between experiment and calculations confirms that the measured CE maps represent the intrinsic electronic structures of ErTe₃, and that the electronic structures of ErTe₃ are described well by the DFT calculations.

Figure 3 shows the ARPES image plots of ErTe₃ along three high-symmetry directions obtained at $h\nu = 104$ eV [37] by using the LH polarization. In Fig. 3(a) is shown the schematic drawing for the LH polarization geometry. Figures 3(b)–3(d) show the ARPES image plots of ErTe₃ along $\bar{X}\bar{\Gamma}\bar{X}$, $\bar{M}\bar{X}\bar{M}$, and $\bar{M}\bar{\Gamma}\bar{M}$, respectively. As shown in Fig. 3, the measured ARPES data are very good in quality so that they can be considered to represent the intrinsic features of ErTe₃. The flat bands at $E_i \sim -6$ eV are Er 4*f* states [20,25] corresponding to the low BE peak shown in Fig. 1. Very dispersive bands for -5 eV $\leq E_i \leq 0$ eV are Te 5*p* states. This interpretation is confirmed by the comparison with the calculated band structures, shown in Figs. 3(e)–3(h).

To understand the microscopic origin of the bands observed in ARPES, we have performed DFT calculations for the normal-phase ErTe₃ (i.e., not considering the CDW distortion) treating Er 4*f* states as core electrons. The calculated band structures along several high-symmetry lines are shown in Fig. 3(e). As described above, these bands represent mainly Te 5*p* states. In Figs. 3(f)–3(h) are shown the comparison between the measured ARPES and the calculated band structures along $\bar{X}\bar{\Gamma}\bar{X}$, $\bar{M}\bar{X}\bar{M}$, and $\bar{M}\bar{\Gamma}\bar{M}$, respectively, superposed onto each other [38]. Most of the large energy-scale band structures agree very well between experiment and

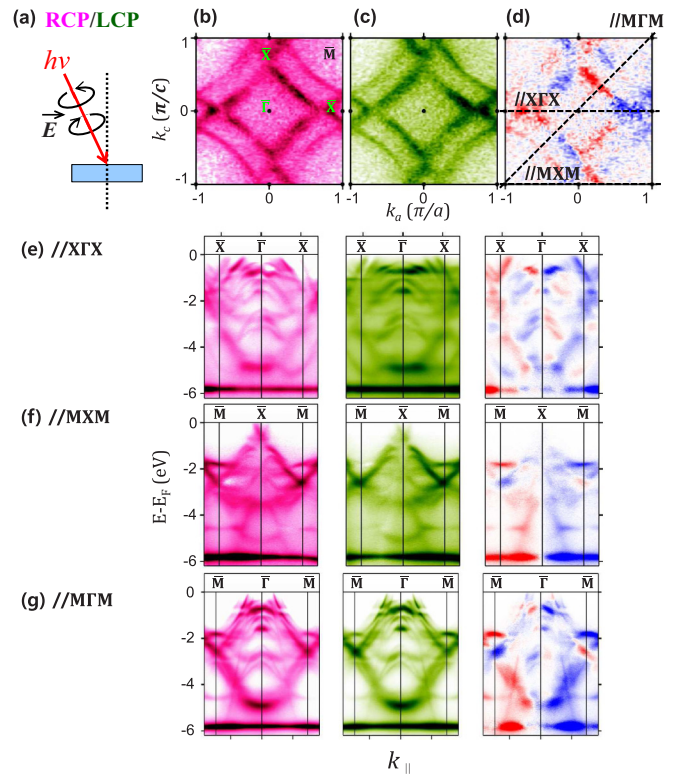


FIG. 4. Circular-dichroism (CD) FS and ARPES of ErTe₃. (a) The schematic drawing for the RCP/LCP geometry. (b)–(d) FS/CE maps of ErTe₃ obtained with the RCP photons (red), the LCP photons (green), and the difference between them [corresponding to the CD map (denoted in red and blue)]. All data were obtained with $h\nu = 76$ eV and at $T \approx 80$ K. In (d), dotted lines represent the three symmetry lines along which CD-ARPES data are obtained, as shown in (e)–(g). (e) ARPES image plots of ErTe₃ along $\bar{X}\bar{\Gamma}\bar{X}$ obtained with the RCP and LCP and the difference between them ($CD \equiv RCP - LCP$). (f), (g) Similarly along $\bar{M}\bar{X}\bar{M}$ and $\bar{M}\bar{\Gamma}\bar{M}$, respectively. All ARPES data were obtained at $h\nu = 104$ eV and at $T \approx 80$ K. In CD FS and ARPES, red and blue colors represent the stronger RCP intensity and the stronger LCP intensity, respectively.

calculations. The flat band at $E_i \approx -6$ eV is missing in the DFT calculations because Er 4*f* electrons are treated as core electrons in the calculations. On the other hand, the calculated band structures agree better with the measured ARPES bands if the calculated bands are shifted down (nonlinearly) by $\sim 0.2 - 0.5$ eV. Such shifts are consistent qualitatively with the shifting E_i 's upward in comparison between the calculated and measured CEs shown in Fig. 2.

Figure 4 shows the effect of CD in the FS and ARPES of ErTe₃ obtained at $h\nu = 76$ eV and at $T \approx 80$ K. In Fig. 4(a) is shown the schematic drawing for the right-circularly polarized (RCP) and left-circularly polarized (LCP) measurement geometry. Figures 4(b) and 4(c) show the FSs measured with the RCP and LCP photons, respectively. Figure 4(d) shows the difference between RCP and LCP FSs corresponding to the CD FS ($CD \equiv RCP - LCP$). Red and blue colors in CD FS denote positive and negative signals in the difference, respectively, so they represent the stronger RCP intensity and stronger LCP intensity, respectively.

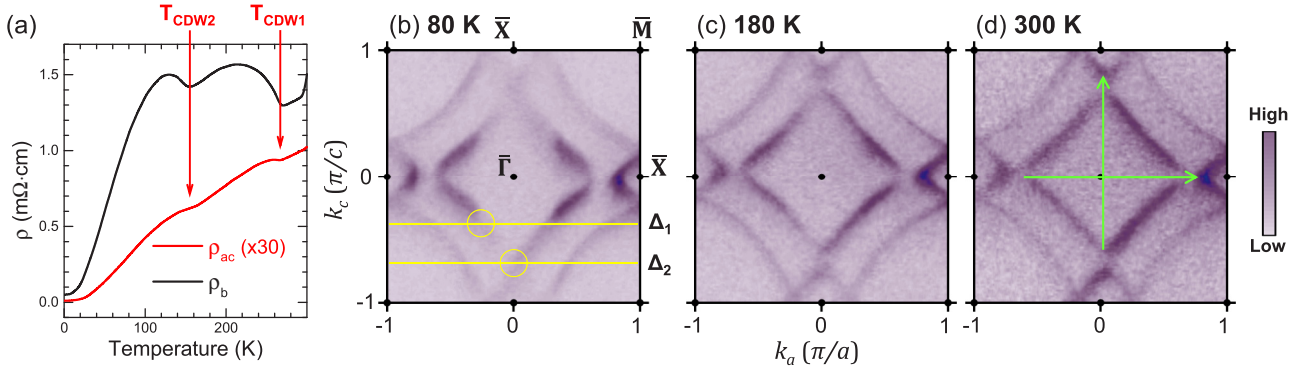


FIG. 5. T -dependent FS of ErTe_3 . (a) T -dependent resistivity $\rho(T)$ of ErTe_3 plotted from the data in Ref. [10] ($T_{CDW1} = 265$ K and $T_{CDW2} = 155$ K). (b)–(d) The FSs measured at $T = 80$, 180, and 300 K, respectively, obtained by using 76 eV LH. Two yellow solid lines in (b) denote the cuts, along which T -dependent near- E_F ARPES data are shown in Figs. 6 and 7. Green arrows in (d) represent the FS nesting vectors, $Q_c \approx 5/7 c^*$ along c^* and $Q_a \approx 5/7 a^*$ along a^* . See text for the details.

The investigation of circular dichroism (CD) in ARPES is very useful because the observed CD reflects the chirality of the system or the chiral orbital and spin polarizations of the electronic states of the system [39]. Technically, however, there are also extrinsic effects in CD-ARPES measurements, mainly due to the geometrical effect [40,41]. So it is important to separate out intrinsic effects from extrinsic effects in CD data. But this process is not trivial. Since we do not have a good scheme to remove the geometric effect in the measured CD data for ErTe_3 , no extraction has been done on these data shown in Fig. 4.

In the CD FS in Fig. 4(d), dotted lines represent three symmetry lines along which ARPES data shown in Figs. 4(e)–4(g) are obtained. Figure 4(e) shows the ARPES image plots along $\bar{X}\bar{\Gamma}\bar{X}$ obtained with the RCP (red color) and the LCP (green color) and CD. Similarly, Figs. 4(f) and 4(g) show those along $\bar{M}\bar{X}\bar{M}$ and $\bar{M}\bar{\Gamma}\bar{M}$, respectively. The observed CD effect in ARPES is consistent with that in the CD FS [see Fig. 4(d)]. The CD ARPES data along $\bar{X}\bar{\Gamma}\bar{X}$, $\bar{M}\bar{X}\bar{M}$, and $\bar{M}\bar{\Gamma}\bar{M}$ show mostly stronger RCP for the left side and stronger LCP for the right side, in particular for the flat bands around -6 eV and those around -2 eV. Some dispersive bands near \bar{X} and $\bar{\Gamma}$ at around -1 eV exhibit the opposite CD effect, i.e., stronger LCP for the left side and stronger RCP for the right side.

Note that the observed CD effects in ARPES are very similar to one another even for different symmetry directions, suggesting that the observed CD effects are mainly due to the geometric effect. Hence the very weak CD effect in both CD FS and CD ARPES implies that the effect of the chiral orbital and spin polarizations in the Te $5p$ states of ErTe_3 is not strong. Nevertheless, further investigation on the effect of CD in ARPES both experimentally and theoretically will be important for future study.

Now we will discuss the T dependence of the CDW gap in ErTe_3 . Figure 5 shows the T -dependent FS of ErTe_3 obtained at $h\nu = 76$ eV by using LH polarization. These FSs are plotted by integrating $E_i = 0$ eV ± 10 meV. Two yellow solid lines in Fig. 5(b), labeled as the first energy gap (Δ_1) and the second energy gap (Δ_2), denote the cuts along which the T -dependent near- E_F ARPES data were obtained (see Figs. 6 and 7). These cuts are selected because the gap features are observed at low T ($T = 80$ K) below the second CDW transition ($T_{CDW2} \approx$

155 K). Two yellow circles denote the points where the energy gaps of Δ_1 and Δ_2 are observed at low T . The position of Δ_1 is consistent with the large gap position observed in Ref. [13]. In this figure, we have selected three temperatures that represent three different phases, such as $T = 80$ K, $T = 180$ K, and $T = 300$ K (note that $T_{CDW2} \approx 155$ K and $T_{CDW1} \approx 265$ K). To show that the selected temperatures belong to three different phases more clearly, the T dependence of the resistivity $\rho(T)$ of ErTe_3 is plotted in Fig. 5(a), the data of which were adopted from Ref. [10].

The T -dependent FSs in Fig. 5 do not reveal much variance, except that the gap feature along Δ_1 disappears as T increases (i.e., the FSs become fully connected with increasing T). A similar trend is revealed along Δ_2 . Note that the second gap in Δ_2 arises mostly from the crossing of quasi-1D bands along k_a and k_c due to band hybridization [see Fig. 2(b)]. The T -dependent feature along Δ_1 implies closing of the energy gaps with increasing T . Considering that the FSs are plotted by integrating $E_i = 0$ eV ± 10 meV, this observation suggests that the size of the CDW energy gap (Δ_1), if it exists, is less than ~ 20 meV, which is smaller than the experimental resolution in this work.

The FS of ErTe_3 in the CDW phase at $T = 80$ K ($T < T_{CDW2}$) exhibits twofold symmetric features [see Fig. 5(b)], mainly in intensity modulation. This feature is similar to but weaker than that of PrTe_3 [20]. In PrTe_3 , the twofold symmetric FS in the CDW phase was found to represent the 7×1 FS reconstruction in the CDW phase [20]. It was found that the local distortions of Te ions in PrTe_3 were described by either the 7×1 oligomers or a sinusoidal function with $Q \approx 5/7 c^*$ (Q : the CDW modulation vector, $c^* \equiv 2\pi/c$).

Hence, the similarity in the CDW-induced FSs of ErTe_3 and PrTe_3 suggests that the CDW modulation vector in ErTe_3 is also likely to be $Q_c \approx 5/7 c^*$ ($Q_a \approx 5/7 a^*$ along a^*). In fact, this Q vector is close to the nesting vector connecting the corners of inner-diamond FS at $T = 300$ K along c^* or a^* [denoted as green vectors in Fig. 5(d)]. Nevertheless, the FS reconstruction in the CDW phase of ErTe_3 seems to be weaker than in PrTe_3 because the twofold symmetric features in the CDW FS of ErTe_3 appear only as the intensity modulation in the FS. In addition, the major shape of the FS does not change with increasing T across T_{CDW2} and T_{CDW1} , indicating

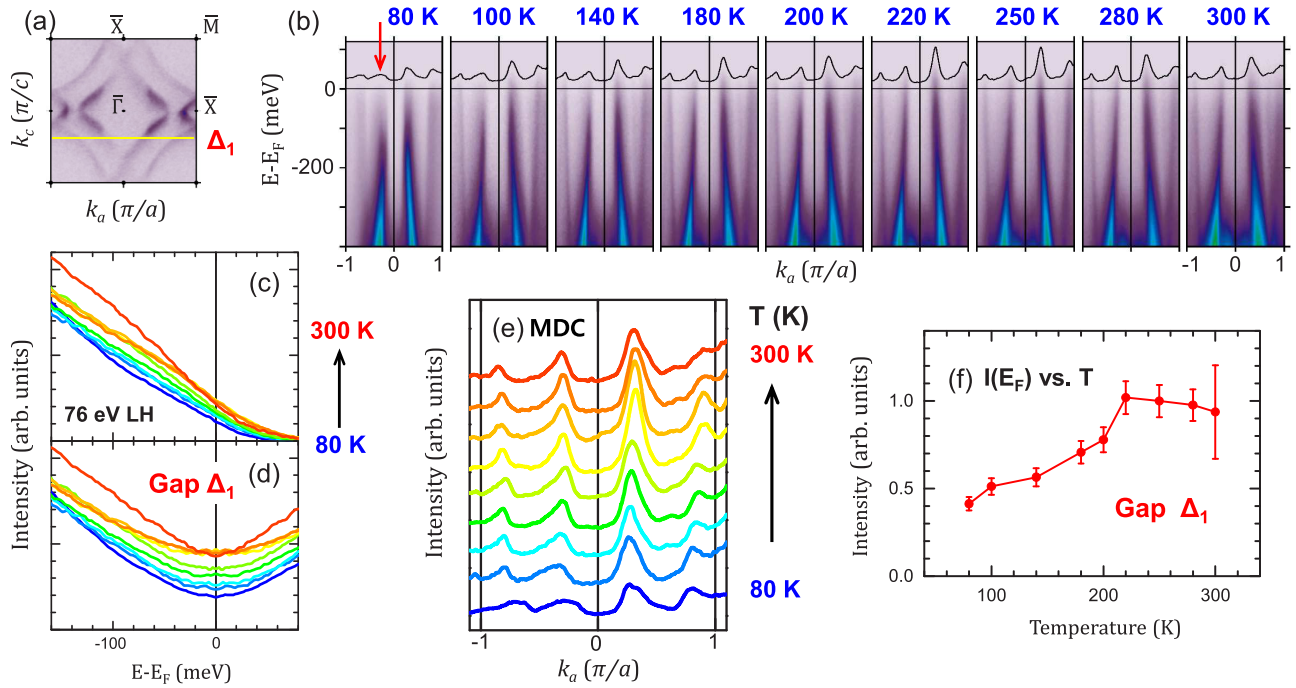


FIG. 6. T -dependent near- E_F ARPES of ErTe₃ for the first gap (Δ_1) feature. (a) $T = 80$ K FS of ErTe₃, where the line (Δ_1) is denoted in yellow, along which T -dependent near- E_F ARPES spectra are obtained. (b) ARPES image plots along Δ_1 for selected temperatures. On top of each ARPES, the corresponding MDC at E_F is displayed. (c) T -dependent EDCs from 80 to 300 K for the first gap that is marked with a red arrow in the 80 K ARPES of Fig. 6(b). (d) Symmetrized T -dependent EDCs. These data are obtained from the EDCs shown in (c) after being divided by a broadened FD distribution function and then symmetrized for the above- E_F region. (e) Stack of MDC images of the E_F states from 80 to 300 K along Δ_1 . (f) T dependence of the E_F weight of the EDC spectra [shown in (c)] with error bars being denoted. All data were obtained at $h\nu = 76$ eV by using the LH polarization.

a weak CDW distortion in ErTe₃. This finding suggests the partial opening of the CDW gap only in a small region of the k space.

Figures 6 and 7 show the T -dependent near- E_F ARPES of ErTe₃ from 80 to 300 K for the first gap (Δ_1) and the second gap (Δ_2) features, respectively. These data were obtained at $h\nu = 76$ eV by using LH polarization. Figure 6(a) shows the $T = 80$ K FS of ErTe₃, where the line Δ_1 is denoted in yellow along which T -dependent near- E_F ARPES spectra are obtained. Figure 6(b) shows ARPES image plots along Δ_1 for selected temperatures, revealing that the states near E_F become stronger with increasing T . This trend is also observed in the corresponding momentum distribution curve (MDC) at E_F that is displayed on top of each ARPES, reflecting the gap closing with increasing T . Figure 6(c) shows T -dependent energy distribution curves (EDCs) for the first gap, marked with an arrow (red) in the 80 K ARPES image of Fig. 6(b). Figure 6(c) reveals the increasing weight at E_F with increasing T . To show this feature more clearly, we have divided the EDCs by the Fermi-Dirac (FD) distribution function convoluted with the instrumental resolution as a rough approximation to the density of states (DOS), then we have symmetrized the FD-divided results with respect to E_F . Such symmetrized T -dependent EDCs are shown in Fig. 6(d). Figures 6(e) and 6(f) show T -dependent MDCs along Δ_1 and T -dependent E_F weight of the EDC spectra, respectively. All these figures confirm the increasing DOS at E_F with increasing T . Even at $T = 80$ K, however, the EDC exhibits the finite DOS, and the slopes of the ARPES bands near E_F do not

exhibit a kink feature that is expected for the CDW formation. Similar features are observed for the second gap Δ_2 shown in Fig. 7.

Considering that ErTe₃ has two-step CDW transitions, it is rather puzzling that no clear changes are observed in the T -dependent ARPES/FS across T_{CDW1} and T_{CDW2} . Such features might be understood as due to the very weak and only partial CDW formation in ErTe₃. Despite the expected CDW distortions of ErTe₃ in the ac plane of the Te(2)-Te(3) sheets, $\rho_{ac}(T)$ of ErTe₃ reveals only very weak slope changes at T_{CDW1} and T_{CDW2} [see Fig. 5(a)], which suggests very weak CDW formation in ErTe₃. On the other hand, $\rho_b(T)$ of ErTe₃ along the b axis reveals just small dips at T_{CDW1} and T_{CDW2} . Hence our findings in T -dependent FS and ARPES data seem to reflect the weak and only partial CDW formations in ErTe₃.

The weaker CDW-induced FS reconstruction in ErTe₃ than that in PrTe₃ suggests that an important factor of CDW-modulations in R Te₃ is probably the different ionic sizes of R ions and the corresponding volume difference. Namely, the smaller volume of ErTe₃ than that of PrTe₃ causes not only the larger bilayer splitting of Te 5 p states at E_F but also the larger dispersion along b^* (weakening the 2D nature), both of which will reduce the FS nesting feature. Furthermore, due to the smaller volume of ErTe₃, the DOS at E_F will also be reduced. All these factors give rise to the weaker CDW-induced FS reconstruction in ErTe₃. As to the two-step CDW transitions in ErTe₃, $\rho(T)$ in the ac plane exhibits very weak changes only [see Fig. 5(a)], suggesting an opening of the partial energy gaps only in a small region of the k space. Hence, such

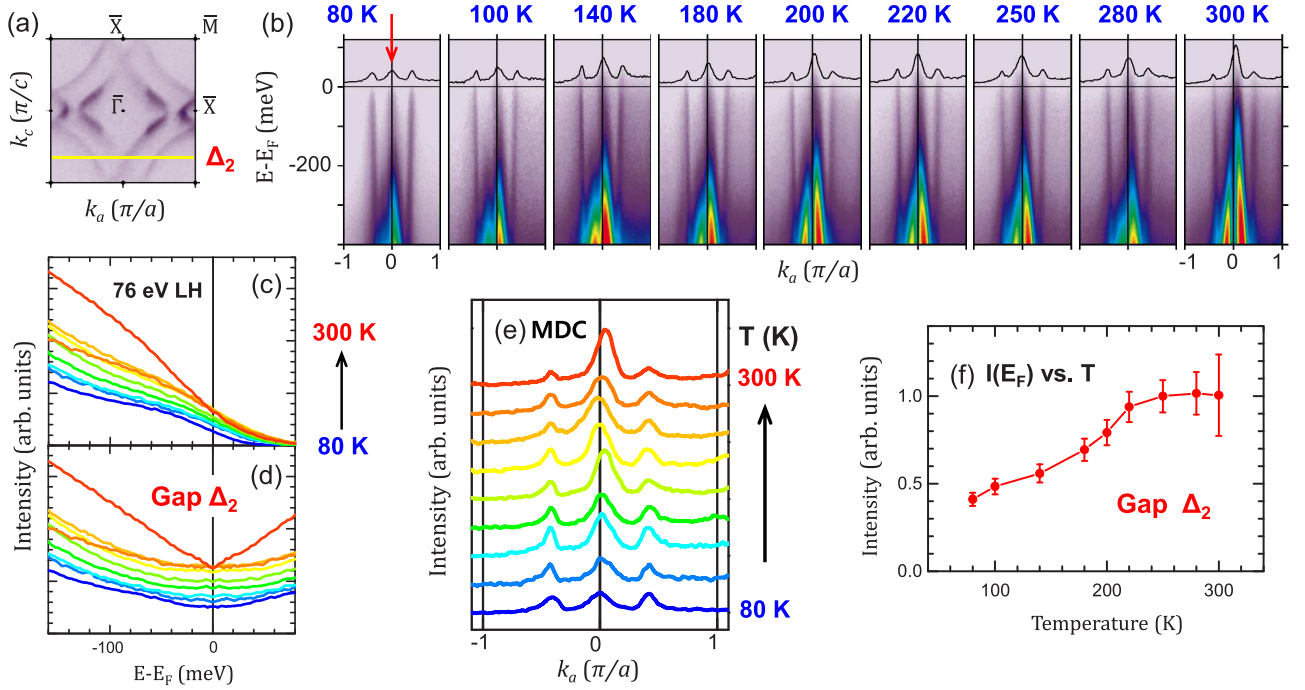


FIG. 7. T -dependent near- E_F ARPES of ErTe_3 for the second gap (Δ_2) feature. (a) $T = 80$ K FS of ErTe_3 , where the line (Δ_2) is denoted in yellow along which T -dependent near- E_F ARPES spectra are obtained. (b) ARPES image plots along Δ_2 for selected temperatures. On top of each ARPES, the corresponding MDC at E_F is displayed. (c) T -dependent EDC spectra from 80 to 300 K for the second gap that is marked with a red arrow in the 80 K ARPES of (b). (d) Symmetrized T -dependent EDCs for the data shown in (c). (e) Stack of MDC images of the E_F states from 80 to 300 K along Δ_2 . (f) T dependence of the E_F weight of the EDC spectra [shown in (c)] with error bars being denoted. All data were obtained at $h\nu = 76$ eV by using the LH polarization.

effects will be delicate to be observed in T -dependent ARPES experiment.

In order to address an important issue in $R\text{Te}_3$ exhibiting two-step CDW transitions for heavy R elements, we adopt the idea of the previous report [42] that is consistent with our findings, as described below. According to a nearly tetragonal structure in $R\text{Te}_3$, there exist two competing FS nesting vectors of Q_c and Q_a ($Q_c \approx Q_a$) along c^* and a^* , respectively. Then, due to the lattice strain energy, one direction may be selected first for the CDW transition [42]. Since the FS nesting for heavy $R\text{Te}_3$ is far less perfect than for light $R\text{Te}_3$ owing to the smaller volumes of heavy $R\text{Te}_3$'s than those of light $R\text{Te}_3$'s, there remains the possibility of the second CDW transition to occur even after the first CDW transition. This might be the reason for the two-step transitions for $R = \text{Dy-Tm}$, while only single-step transitions for $R = \text{Ce-Tb}$. Imperfect nesting due to the smaller volumes for heavy $R\text{Te}_3$, together with the reduced DOS at E_F , is consistent with the reduced first transition temperature T_{CDW1} for heavy $R\text{Te}_3$ than for light $R\text{Te}_3$.

It is worthwhile to note that the FS of CeTeSb is very similar to that of ErTe_3 [43]. $R\text{TeSb}$ (R : rare-earth ion) family has the ZrSiS-type crystal structure in which $R\text{Te}$ bilayers are separated by a square net of Sb, and these layers are stacked along c (corresponding to b in ErTe_3). This crystal structure is similar to that of ErTe_3 . Replacement of one Te layer in CeTe_2 by an Sb layer in CeTeSb results in a hole-doping effect, which is similar to the case for CeTe_3 behaving as hole-doped CeTe_2 due to the extra Te layer. A larger hole-doping effect in CeTeSb naturally gives rise to a bit larger FS at Γ than

in CeTe_2 and CeTe_3 . Indeed, the CDW transition has been observed in CeTeSb [43]. Interestingly, these $R\text{TeSb}$ compounds are considered as Dirac nodal-line semimetals, which allow a variety of topological/trivial states to be controlled through band-structure engineering [44–46]. Therefore, the above discussion on ErTe_3 might be extended to $R\text{SbTe}$, which could be checked via ARPES investigation on $R\text{SbTe}$ series.

IV. CONCLUSION

The electronic structures of a double-CDW-transition system ErTe_3 have been investigated by performing dichroic ARPES, T -dependent ARPES, and RPES measurements for high-quality single crystals. Er $4d \rightarrow 4f$ RPES study of ErTe_3 reveals that the Er $4f$ states do not contribute directly to the CDW formation. The shadow bands and the corresponding shadow FSs, due to the band folding arising from the inter-layer interaction between R-Te(1) and Te(2)-Te(3) layers, are clearly observed.

Twofold symmetric FS is observed in the CDW phase of ErTe_3 , which is similar to that of PrTe_3 , suggesting the CDW modulation vector of $Q \approx 5/7 c^* \approx 5/7 a^*$ in ErTe_3 . However, the features of the CDW-induced FS reconstruction are very weak, and the ARPES data in the CDW phase exhibit no kinks expected for the CDW formation. The measured FSs and ARPES data in the CDW phase agree very well with the DFT calculations for the non-CDW phase, which confirms the very weak and only partial CDW-induced FS reconstruction in ErTe_3 . Very weak and similar CD is observed along different symmetry lines in FS and ARPES, suggesting weak

chiral orbital and spin polarizations in the Te $5p$ states and the geometric effect of the ARPES experimental setup as its origin.

T -dependent FS and ARPES measurements reveal closing of the CDW gap with increasing T , but no clear changes across $T_{\text{CDW}2}$ and $T_{\text{CDW}1}$. The origin of the very weak CDW reconstruction in ErTe_3 is likely to be the small ionic sizes of Er ions and the concomitant small volume, which produce imperfect FS nesting and reduced DOS at E_F . The very weak FS reconstruction at the first CDW transition along c^* at $T_{\text{CDW}1}$ is considered to be a reason why there exists a second CDW transition further along a^* at $T_{\text{CDW}2}$, which elucidates

the observed double CDW transitions in ErTe_3 . To confirm this conjecture, further theoretical investigation would be very useful.

ACKNOWLEDGMENTS

This work was supported by the National Research Foundation (NRF) of Korea (No. 2019R1A2C1004929; No. 2017R1A2B4005175), MSIP, PAL, and in part by the Research Fund 2021 of the Catholic University of Korea. K.K. was supported by KAERI internal R&D Program (No. 524460-21).

-
- [1] W. Kohn, *Phys. Rev. Lett.* **2**, 393 (1959).
- [2] N. W. Ashcroft and N. D. Mermin, *Solid State Physics* (Holt, Rinehart and Winston, 1976).
- [3] J. Voit, L. Perfetti, F. Zwick, H. Berger, G. Margaritondo, G. Grüner, H. Höchst, and M. Grioni, *Science* **290**, 501 (2000).
- [4] T. Kasuya, M. H. Jung, and T. Takabatake, *J. Magn. Magn. Mater.* **220**, 235 (2000).
- [5] K. Rossnagel, *J. Phys.: Condens. Matter* **23**, 213001 (2011).
- [6] M. Grioni, I. Vobomik, F. Zwick, and G. Margaritondo, *J. Electron Spectrosc. Relat. Phenom.* **100**, 313 (1999).
- [7] P. Aebi, T. Pillo, H. Berger, and F. Levy, *J. Electron Spectrosc. Relat. Phenom.* **117-118**, 433 (2001).
- [8] H. Yao, J. A. Robertson, E. A. Kim, and S. A. Kivelson, *Phys. Rev. B* **74**, 245126 (2006).
- [9] H. J. Kim, C. D. Malliakas, A. T. Tomic, S. H. Tessmer, M. G. Kanatzidis, and S. J. L. Billinge, *Phys. Rev. Lett.* **96**, 226401 (2006).
- [10] N. Ru, C. L. Condon, G. Y. Margulis, K. Y. Shin, J. Laverock, S. B. Dugdale, M. F. Toney, and I. R. Fisher, *Phys. Rev. B* **77**, 035114 (2008).
- [11] N. Ru, J.-H. Chu, and I. R. Fisher, *Phys. Rev. B* **78**, 012410 (2008).
- [12] A. Fang, N. Ru, I. R. Fisher, and A. Kapitulnik, *Phys. Rev. Lett.* **99**, 046401 (2007).
- [13] R. G. Moore, V. Brouet, R. He, D. H. Lu, N. Ru, J.-H. Chu, I. R. Fisher, and Z.-X. Shen, *Phys. Rev. B* **81**, 073102 (2010).
- [14] N. Lazarevic, Z. V. Popovic, R. Hu, and C. Petrovic, *Phys. Rev. B* **83**, 024302 (2011).
- [15] H.-M. Eiter, M. Lavagnini, R. Hackl, E. A. Nowadnick, A. F. Kemper, T. P. Devereaux, J.-H. Chu, J. A. Analytis, I. R. Fisher, and L. Degiorgi, *Proc. Natl. Acad. Sci. USA* **110**, 64 (2013).
- [16] G.-H. Gweon, J. D. Denlinger, J. A. Clack, J. W. Allen, C. G. Olson, E. D. DiMasi, M. C. Aronson, B. Foran, and S. Lee, *Phys. Rev. Lett.* **81**, 886 (1998).
- [17] H. Komoda, T. Sato, S. Souma, T. Takahashi, Y. Ito, and K. Suzuki, *Phys. Rev. B* **70**, 195101 (2004).
- [18] J. Laverock, S. B. Dugdale, Z. Major, M. A. Alam, N. Ru, I. R. Fisher, G. Santi, and E. Bruno, *Phys. Rev. B* **71**, 085114 (2005).
- [19] V. Brouet, W. L. Yang, X. J. Zhou, Z. Hussain, N. Ru, K. Y. Shin, I. R. Fisher, and Z.-X. Shen, *Phys. Rev. Lett.* **93**, 126405 (2004); V. Brouet, W. L. Yang, X. J. Zhou, Z. Hussain, R. G. Moore, R. He, D. H. Lu, Z. X. Shen, J. Laverock, S. B. Dugdale, N. Ru, and I. R. Fisher, *Phys. Rev. B* **77**, 235104 (2008), and references therein.
- [20] E. Lee, D. H. Kim, H. W. Kim, J. D. Denlinger, H. Kim, J. Kim, K. Kim, B. I. Min, B. H. Min, Y. S. Kwon, and J.-S. Kang, *Sci. Rep.* **6**, 30318 (2016).
- [21] N. Ru and I. R. Fisher, *Phys. Rev. B* **73**, 033101 (2006).
- [22] J. A. W. Straquadine, F. Weber, S. Rosenkranz, A. H. Said, and I. R. Fisher, *Phys. Rev. B* **99**, 235138 (2019).
- [23] P. Blaha, K. Schwarz, F. Tran, R. Laskowski, G. K. H. Madsen, and L. D. Marks, *J. Chem. Phys.* **152**, 074101 (2020).
- [24] J. W. Allen, S.-J. Oh, O. Gunnarsson, K. Schönhammer, M. B. Maple, M. S. Torikachvili, and I. Lindau, *Adv. Phys.* **35**, 275 (1987).
- [25] F. Gerken, A. S. Flodstrom, J. Barth, L. I. Johnsson, and C. Kunz, *Phys. Scr.* **32**, 43 (1985).
- [26] P. A. Cox, Y. Baer, and C. K. Jorgensen, *Chem. Phys. Lett.* **22**, 433 (1973); P. A. Cox, *Struc. Bond.* **24**, 59 (1975).
- [27] H. Kim, K. Kim, and B. I. Min (unpublished).
- [28] E. Lee, D. H. Kim, J. D. Denlinger, J. Kim, K. Kim, B. I. Min, B. H. Min, Y. S. Kwon, and J.-S. Kang, *Phys. Rev. B* **91**, 125137 (2015).
- [29] It is expected that the relative photoemission intensity from *surface* and *bulk* vary for different cleaves.
- [30] J.-S. Kang, C. G. Olson, Y. S. Kwon, J. H. Shim, and B. I. Min, *Phys. Rev. B* **74**, 085115 (2006).
- [31] J. K. Burdett and S. Lee, *J. Am. Chem. Soc.* **105**, 1079 (1983).
- [32] J. H. Shim, J.-S. Kang, and B. I. Min, *Phys. Rev. Lett.* **93**, 156406 (2004).
- [33] E. DiMasi, B. Foran, M. C. Aronson, and S. Lee, *Phys. Rev. B* **54**, 13587 (1996).
- [34] A. Kikuchi, *J. Phys. Soc. Jpn.* **67**, 1308 (1998).
- [35] K. Stöwe, *J. Alloy Compd.* **307**, 101 (2000); *J. Solid State Chem.* **149**, 155 (2000).
- [36] J.-S. Kang, D. H. Kim, H. J. Lee, J. Hwang, H.-K. Lee, H.-D. Kim, B. H. Min, K. E. Lee, Y. S. Kwon, J. W. Kim, K. Kim, B. H. Kim, and B. I. Min, *Phys. Rev. B* **85**, 085104 (2012).
- [37] Since ErTe_3 is quasi-2D, it is not crucial to determine exactly the photon energies ($h\nu$'s corresponding to the high-symmetry planes).
- [38] In this comparison, the calculated band structures are not shifted, different from the comparison for FS/CE shown in Fig. 2. It is because the amount of the shift in the calculated bands appears to be nonlinear, i.e., the amount of the shift varies for different bands as well as for different k positions.
- [39] Y. A. Bychkov and É. I. Rashba, *J. Exp. Theor. Phys.* **39**, 78 (1984).

- [40] A. Kaminski, S. Rosenkranz, H. M. Fretwell, J. C. Campuzano, Z. Li, H. Raffy, W. G. Cullen, H. You, C. G. Olson, C. M. Varma, and H. Höchst, *Nature (London)* **416**, 610 (2002).
- [41] S. Cho, J.-H. Park, J. Hong, J. Jung, B. S. Kim, G. Han, W. Kyung, Y. Kim, S.-K. Mo, J. D. Denlinger, J. H. Shim, J. H. Han, C. Kim, and S. R. Park, *Phys. Rev. Lett.* **121**, 186401 (2018).
- [42] R. G. Moore, W. S. Lee, P. S. Kirchman, Y. D. Chuang, A. F. Kemper, M. Trigo, L. Patthey, D. H. Lu, O. Krupin, M. Yi, D. A. Reis, D. Doering, P. Denes, W. F. Schlotter, J. J. Turner, G. Hays, P. Hering, T. Benson, J.-H. Chu, T. P. Devereaux *et al.*, *Phys. Rev. B* **93**, 024304 (2016).
- [43] P. Li, B. Lv, Y. Fang, W. Guo, Z. Wu, Y. Wu, C.-M. Cheng, D. Shen, Y. Nie, L. Petaccia, C. Cao, Z.-A. Xu, and Y. Liu, *Sci. China Phys. Mech.* **64**, 237412 (2021).
- [44] L. M. Schoop, A. Topp, J. Lippmann, F. Orlandi, L. MÜchler, M. G. Vergniory, Y. Sun, A. W. Rost, V. Duppel, M. Krivenkov, S. Sheoran, P. Manuel, A. Varykhalov, B. Yan, R. K. Kremer, C. R. Ast, and B. V. Lotsch, *Sci. Adv. Phys.* **4**, eaar2317 (2018).
- [45] A. Weiland, D. G. Chaparro, M. G. Vergniory, E. Derunova, J. Yoon, I. W. H. Oswald, G. T. McCandless, M. Ali, and J. Y. Chan, *APL Mater.* **7**, 101113 (2019).
- [46] B. Lv, J. Chen, L. Qiao, J. Ma, X. Yang, M. Li, M. Wang, Q. Tao, and Z.-A. Xu, *J. Phys.: Condens. Matter* **31**, 355601 (2019).